South Asian populations show shared histories of archaic admixture, we find significant evidence of differential Neandertal admixture between some European and East Asian populations (figs. S15 to S17).

The density of surviving Neandertal sequences across the genome is heterogeneous (*11*), and regions that are strongly depleted of Neandertal ancestry may represent loci where archaic sequences were deleterious in hybrid individuals and were purged from the population. To quantify how unusual Neandertal depleted regions are under neutral models, we performed coalescent simulations (*14*), focusing on individuals of European and East Asian ancestry whose demographic histories are known in most detail. Depletions of Neandertal sequences that extend ≥8 Mb are significantly enriched in the observed compared with simulated data (permutation $P < 0.01$) (Fig. 4A and fig. S18). Neandertal depleted regions that span at least 8 Mb are also significantly (Kolmogorov-Smirnov test, $P < 10^{-15}$) depleted of Neandertal sequences in South Asians and Melanesians (fig. S19 and table S8).

We find significantly more overlap in regions depleted of Neandertal and Denisovan lineages than expected by chance (permutation $P = 0.0008$) (fig. S20 and table S9) (*14*), consistent with recurrent selection against deleterious archaic sequences. Indeed, deserts of archaic sequences tend to exhibit higher levels of background selection (figs. S21 and S22). Regions depleted of archaic lineages are significantly enriched for genes expressed in specific brain regions, particularly in the developing cortex and adult striatum (permutation $P < 0.05$) (table S10). A large region depleted of archaic sequences spans 11 Mb on chromosome 7 and contains the *FOXP2* gene (Fig. 4B), which has been associated with speech and language (*23*). This region is also significantly enriched for genes associated with autism spectrum disorders (Fisher's exact test, $P = 0.008$) (*14*). Although our data show that large regions depleted of archaic ancestry are inconsistent with neutral evolution, mechanisms other than selection, such as structural variation, could also contribute to the appearance of archaic deserts, and thus additional work is necessary to fully understand the origins of such regions.

We identified putative adaptively introgressed sequences in Melanesians by identifying archaic haplotypes at unusually high frequencies, as determined by coalescent simulations under a wide variety of neutral demographic models (*14*). At a frequency threshold of 0.56, corresponding to the 99th percentile of simulated data, we identified 21 independent candidate regions for adaptive introgression (Fig. 4C and table S12). Fourteen are of Neanderthal origin, three are Denisovan, three are ambiguous, and one segregates both Neanderthal and Denisovan haplotypes. Six regions do not contain any protein-coding genes, and seven high-frequency archaic haplotypes span only a single gene (table S12). High-frequency archaic haplotypes overlap several metabolism-related genes, such as *GCG* (a hormone that increases blood glucose levels) and *PLPP1* (a membrane protein involved in lipid metabolism). Moreover, five regions either span or are adjacent to immune-related genes, including a haplotype encompassing *GBP4* and *GBP7* (Fig. 4D), which are induced by interferon as part of the innate immune response.

Substantial amounts of Neandertal and Denisovan DNA can now be robustly identified in the genomes of present-day Melanesians, allowing new insights into human evolutionary history. As genome-scale data from worldwide populations continue to accumulate, a nearly complete catalog of surviving archaic lineages may soon be within reach. Key challenges remain, including evaluating the functional and phenotypic consequences of introgressed sequences and refining estimates on the timing, location, and other characteristics of admixture events. Ultimately, maps of surviving Neandertal, Denisovan, and potentially other hominin (*1*) sequences will help us to interpret patterns of human genomic variation and understand how archaic admixture influenced the trajectory of human evolution.

REFERENCES AND NOTES

1. S. Vattathil, J. M. Akey, *Cell* **163**, 281–284 (2015).
2. R. E. Green *et al.*, *Science* **328**, 710–722 (2010).
3. K. Prüfer *et al.*, *Nature* **505**, 43–49 (2014).
4. D. Reich *et al.*, *Nature* **468**, 1053–1060 (2010).
5. M. Meyer *et al.*, *Science* **338**, 222–226 (2012).
6. M. A. Yang, A. S. Malaspinas, E. Y. Durand, M. Slatkin, *Mol. Biol. Evol.* **29**, 2987–2995 (2012).
7. S. Sankararaman, N. Patterson, H. Li, S. Pääbo, D. Reich, *PLOS Genet.* **8**, e1002947 (2012).
8. J. D. Wall *et al.*, *Genetics* **194**, 199–209 (2013).
9. P. Skoglund, M. Jakobsson, *Proc. Natl. Acad. Sci. U.S.A.* **108**, 18301–18306 (2011).
10. P. Qin, M. Stoneking, *Mol. Biol. Evol.* **32**, 2665–2674 (2015).
11. B. Vernot, J. M. Akey, *Science* **343**, 1017–1021 (2014).
12. S. Sankararaman *et al.*, *Nature* **507**, 354–357 (2014).
13. J. S. Friedlaender *et al.*, *PLOS Genet.* **4**, e19 (2008).
14. Supplementary materials are available on *Science* Online.
15. N. Patterson *et al.*, *Genetics* **192**, 1065–1093 (2012).
16. I. Lazaridis *et al.*, *Nature* **513**, 409–413 (2014).
17. D. Reich, K. Thangaraj, N. Patterson, A. L. Price, L. Singh, *Nature* **461**, 489–494 (2009).
18. V. Plagnol, J. D. Wall, *PLOS Genet.* **2**, e105 (2006).
19. A. Auton *et al.*, *Nature* **526**, 68–74 (2015).
20. M. Sikora *et al.*, *PLOS Genet.* **10**, e1004353 (2014).
21. B. Vernot, J. M. Akey, *Am. J. Hum. Genet.* **96**, 448–453 (2015).
22. B. Y. Kim, K. E. Lohmueller, *Am. J. Hum. Genet.* **96**, 454–461 (2015).
23. T. Maricic *et al.*, *Mol. Biol. Evol.* **30**, 844–852 (2013).

ACKNOWLEDGMENTS

We thank members of the Akey and Pääbo laboratories for helpful feedback related to this work, F. Friedlaender for help in data management, J. Lorenz and J. Madeoy for DNA extractions and purifications, L. Jáuregui for help in figure preparation, and the participants in this study. Whole-genome sequence data have been deposited into the Database of Genotypes and Phenotypes (dbGAP) with the accession number phs001085.v1.p1. This work was supported by an NIH grant (5R01GM110068) to J.M.A., an NSF fellowship (DBI-1402120) to J.G.S., and grants from the Deutsche Forschungsgemeinschaft (SFB1052, project A02) to J.K. and from the Presidential Fund of the Max Planck Society to S.P. Sample collection was supported in part by NSF grants 9601020 and 0413449 to D.A.M. J.M.A. is a paid consultant of Glenview Capital.

SUPPLEMENTARY MATERIALS

www.sciencemag.org/content/352/6282/235/suppl/DC1
Materials and Methods
Figs. S1 to S22
Tables S1 to S12
References (*24*–*73*)

24 November 2015; accepted 29 February 2016
Published online 17 March 2016
10.1126/science.aad9416

BIOPHYSICS

Direct observation of transition paths during the folding of proteins and nucleic acids

Krishna Neupane,[1] Daniel A. N. Foster,[1] Derek R. Dee,[1] Hao Yu,[1] Feng Wang,[2] Michael T. Woodside[1,2]*

Transition paths, the fleeting trajectories through the transition states that dominate the dynamics of biomolecular folding reactions, encapsulate the critical information about how structure forms. Owing to their brief duration, however, they have not previously been observed directly. We measured transition paths for both nucleic acid and protein folding, using optical tweezers to observe the microscopic diffusive motion of single molecules traversing energy barriers. The average transit times and the shapes of the transit-time distributions agreed well with theoretical expectations for motion over the one-dimensional energy landscapes reconstructed for the same molecules, validating the physical theory of folding reactions. These measurements provide a first look at the critical microscopic events that occur during folding, opening exciting new avenues for investigating folding phenomena.

Biomolecular folding is famously complex, involving a diffusive search over a multidimensional conformational energy landscape for the lowest-energy structure (*1*). The most critical parts of the folding pathway, dominating the dynamics, are the transition states, the unstable intermediates through which a molecule must pass when changing conformation (*2*). A key goal in folding studies has been to observe molecules as they traverse a particular

path through the transition states, providing a direct view of the behavior in the transition states. Such transition paths (Fig. 1A) are very short-lived, however, and are moreover inherently a single-molecule phenomenon, features that make them very challenging to observe experimentally. As a result, although transition paths have been studied in computational simulations (*3*, *4*), folding experiments have primarily used indirect means of characterizing transition states (*2*). The inability to observe transition paths has also limited direct experimental tests at the microscopic level of the fundamentally diffusive nature of folding.

Recently, advances in single-molecule methods have enabled the first glimpses of the transition paths in folding reactions. By analyzing photon statistics from high–time-resolution single-molecule fluorescence spectroscopy measurements, the average transit time across transition paths, τ_{tp}, was found for two small proteins, α_3D and a WW domain (*5*, *6*), and upper bounds were determined for the protein GB1 (*5*, *7*) and a DNA hairpin (*8*). Average transition path times were also found indirectly for both protein and nucleic acid folding from force spectroscopy measurements, in which single molecules were unfolded and refolded under tension applied by optical tweezers (*9*), using diffusive theories to determine the value for τ_{tp} expected from the measured energy landscape for folding (*10*–*12*). Statistical features of the transition paths, such as the conditional probability of being on a transition path as a function of the reaction coordinate (*13*), were also investigated, revealing that the folding was well described by one-dimensional (1D) diffusion (*14*). Despite these advances, however, it has not been possible to discern directly the properties of individual transition paths.

Here we describe measurements observing transition paths directly in the folding of single molecules, using high-resolution force spectroscopy. Force spectroscopy is an especially powerful tool for studying transition paths, because many transitions can be measured from a single molecule, yielding robust statistics. We first studied the two-state DNA hairpin 30R50/T4 (Fig. 1B, inset), which has been characterized extensively in previous work (*10*, *14*, *15*), especially through measurements of the energy landscape underlying its folding properties (*16*–*19*). Folding and unfolding transitions of single hairpins connected via DNA handles to beads held in two stiff optical traps (Fig. 1B) were measured in equilibrium at constant trap separation, at a load close to the force required to populate the folded and unfolded states equally, $F_{1/2}$ (*20*). The time resolution of the measurement was improved more than fivefold from previous studies of τ_{tp} (*10*, *11*), to about 6 to 11 μs (fig. S1).

From equilibrium trajectories of the extension of the molecule (Fig. 1C), individual transitions (Fig. 1D, red) were identified as those crossing between boundaries x_1 and x_2 (Fig. 1D, cyan) defining the barrier region separating the folded and unfolded states (Fig. 1D, orange). Examining individual transition paths for unfolding (Fig. 2A) and refolding (Fig. 2B), their duration was found to vary widely, from less than 10 μs to over 100 μs. Moreover, diverse shapes were observed: The speed often varied greatly along the paths, and noticeable pauses occurred at one or more points in the transition. These pauses occurred in the barrier region, providing the first direct visualization of a host of transient, high-energy transition intermediates. In many transitions, the hairpin shuttled back and forth between different extensions, directly demonstrating, at the microscopic level, the diffusive nature of folding.

To test quantitatively the physical picture of folding as a diffusive search, we studied the duration of the transition paths. The transit time for barrier crossing in each transition, t_{tp}, was measured directly from the extension trajectory as the time required to cross from one boundary to the other (Fig. 1D). For consistency, the boundaries were chosen to define the barrier region as the middle half of the total extension change between the folded and unfolded states, Δx_{UF} (*20*). Measuring transit times individually for 24,591 unfolding transitions and 24,600 refolding transitions, the average value, τ_{tp}, was found to be 27 ± 2 μs for unfolding and 28 ± 2 μs for refolding (errors represent SEM). These average times were slower than the upper bound for τ_{tp} estimated previously for a much shorter DNA hairpin (*8*), but similar to the value for an engineered protein (*6*). Notably, τ_{tp} was roughly 1000-times smaller than the lifetimes of the unfolded and folded states. As expected from symmetry under time reversal (*21*), τ_{tp} was the same for both directions.

These results allowed us to test the theory of transition paths experimentally. For example, assuming 1D diffusive motion over a harmonic barrier in the high-barrier limit ($\Delta G^{\ddagger} > 2\ k_BT$), τ_{tp} is related to the diffusion coefficient, D, by

$$\tau_{tp} \approx \frac{\ln(2e^{\gamma}\beta\Delta G^{\ddagger})}{\beta D \kappa_b} \qquad (1)$$

where $\Delta G^{\ddagger}$ is the barrier height, κ_b is the stiffness of the barrier, γ is Euler's constant, and $\beta = 1/k_BT$ is the inverse thermal energy (*7*, *21*). Previously, the measured landscape profile (*16*) and folding/unfolding rates (*15*) for hairpin 30R50/T4 were used to calculate D from Kramers' equation for diffusive barrier crossing (*22*), in turn enabling calculation of τ_{tp} from Eq. 1. These earlier results, τ_{tp} = 30 ± 6 μs for unfolding and 33 ± 8 μs for refolding (*10*), agree very well with those from the direct measurements, validating Eq. 1. Because τ_{tp} is in principle a more robust measure than approaches that estimate D from rates using Kramers' theory (*6*, *23*), we used Eq. 1 to refine the previous estimate of D. Using the barrier parameters from the reconstructed landscape for this hairpin (*16*), $\Delta G^{\ddagger}$ = 9.1 ± 0.1 k_BT and κ_b = 0.29 ± 0.02 k_BT/nm^2, we found D = 4.4 ± 0.4 × 10^5 nm^2/s, which is very close to the value of 4.6 ± 0.5 × 10^5 nm^2/s estimated previously (*10*).

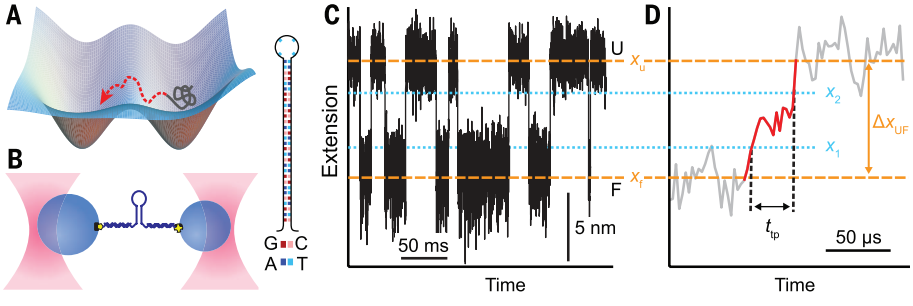

Fig. 1. Transition paths in force spectroscopy measurements. (**A**) Transition paths represent the brief portions of a folding trajectory spent in crossing the barrier between states (red), in contrast to the majority spent fluctuating within one of the potential wells (gray). (**B**) A DNA hairpin attached to handles (dark blue) was linked to beads (blue) held in laser traps (pink) applying tension. (Inset) Hairpin sequence. (**C**) End-to-end extension of a hairpin fluctuating in equilibrium between folded (F) and unfolded (U) states under conditions of constant trap separation. (**D**) Transition paths were identified as the parts of the trajectories (red) moving between U and F (dashed orange lines). The transit time, t_{tp}, was defined as the time required to cross between the boundaries x_1 and x_2 (dotted cyan lines). Here, the transition shows variations in the speed of the barrier crossing, including a brief pause near the center of the barrier region.

Fig. 2. Transition paths for a DNA hairpin. Selection of transition paths for (**A**) unfolding and (**B**) refolding. Boundaries x_1 and x_2 (cyan) demark the barrier region. Transition paths display a wide variety of shapes and transit times.

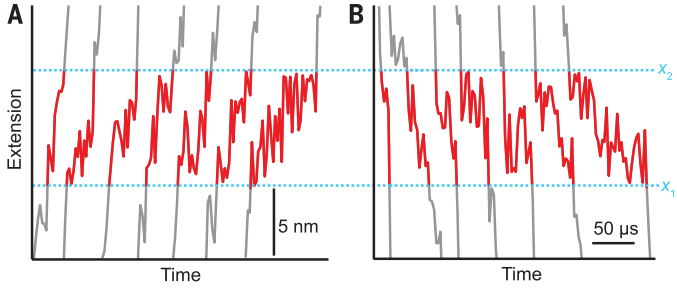

[1]Department of Physics, University of Alberta, Edmonton, Alberta, T6G 2E1, Canada. [2]National Institute for Nanotechnology, National Research Council, Edmonton, Alberta, T6G 2M9, Canada.
*Corresponding author. E-mail: michael.woodside@ualberta.ca

We next tested a proposed relationship between τ_{tp} and kinetic rates (*21*, *24*)

$$\tau_{tp} = \frac{p(TP)}{2k_U P_F} = \frac{p(TP)}{2k_F P_U} \quad (2)$$

where k_F and k_U are the rates for folding and unfolding, respectively; P_F and P_U are the equilibrium probabilities to be in the folded or unfolded states; and p(TP) is the fraction of time spent on transition paths. Each of these quantities could be measured directly from the extension trajectories. Comparing the measured τ_{tp} values with the estimates from Eq. 2 based on folding and unfolding rates (Fig. 3A), we found excellent agreement for both folding and unfolding across a range of forces, from the hairpin being mostly folded ($P_U \sim 0.03$) to mostly unfolded ($P_U \sim 0.8$). This agreement validates Eq. 2; furthermore, it emphasizes that the time-reversal symmetry of τ_{tp} holds across the full range of state occupancies.

Even more interesting than the average transit time is the distribution of the individual transit times, because the variability in transit times reflects the fundamentally statistical nature of the folding process (*1*). The distribution of transit times, $P_{TP}(t)$, for unfolding transitions (Fig. 3B, black) had the same shape as that for refolding (Fig. 3B, green), as expected from the time-reversal symmetry of the problem (*21*). The transit times were broadly distributed, with a peak around 10 μs and a long exponential tail (Fig. 3B, inset). This behavior is similar to that expected for transit across harmonic barriers in the high-barrier limit in the Kramers' regime: $P_{TP}(t)$ is predicted to have the form

$$P_{TP}(t) \approx \frac{\omega_K \sqrt{\beta\Delta G^{\ddagger}}}{1-erf\sqrt{\beta\Delta G^{\ddagger}}} \frac{\exp[-\beta\Delta G^{\ddagger}\coth(\omega_K t/2)]}{\sinh(\omega_K t/2)\sqrt{2\pi\sinh(\omega_K t)}} \quad (3)$$

where $\omega_K = \beta D \kappa_b$ sets the time scale for the decay of the exponential tail (*21*). The exponential tail of $P_{TP}(t)$ on its own can also be approximated (*21*) by

$$P_{TP}(t) \approx 2\omega_K \beta\Delta G^{\ddagger} \exp(-\omega_K t) \quad (4)$$

Fits of the two distributions to Eq. 3 (Fig. 3B, solid lines) and Eq. 4 (Fig. 3B, dashed lines) were barely distinguishable, yielding $\omega_K = 6 \pm 3 \times 10^4\ s^{-1}$ for both folding and unfolding. This result yields $D = 2 \pm 1 \times 10^5\ nm^2/s$, which is close to the values calculated from the measured τ_{tp} using Eq. 1 and estimated from rates via Kramers' theory. However, the barrier height returned by the fit, $\Delta G^{\ddagger} \sim 0.4\ k_B T$, was much lower than that measured directly from landscape reconstructions (*16*–*19*), reflecting the fact that there were more fast transitions than would be expected from the theory for 1D harmonic barriers.

DNA hairpins represent a powerful model system for exploring the physical basis of folding phenomena, but their folding is simpler than that of proteins because they have only secondary structure. We therefore sought to apply the same approach to protein folding. To this end, we focused on a specific structural transition in the prion protein PrP that occurs during the formation of non-native structure in PrP dimers (*20*). This transition undergoes unusually slow conformational diffusion (*25*), making it much easier to measure transit times. The transit times were measured directly from extension trajectories, using the same criterion as for the hairpins. Here, however, the transit times were much longer, up to the millisecond scale (Fig. 4A). Once again, the transit times for both unfolding and refolding were broadly distributed with an exponential tail, and the same distribution was observed for both unfolding (Fig. 4B, black) and refolding (Fig. 4B, green).

As expected, τ_{tp} was again the same for unfolding and refolding: 0.5 ± 0.1 ms from 1766 transitions. These values also matched (within error) the value expected from Eq. 1, $\tau_{tp} = 1 \times 10^{0 \pm 0.3}$ ms, which was calculated (*25*) based on the properties of the energy landscape reconstructed for this transition ($\Delta G^{\ddagger} = 4 \pm 1\ k_B T$ and $\kappa_b = 2 \pm 0.5\ k_B T/nm^2$ at $F_{1/2}$) and the diffusion coefficient estimated from the rates using Kramers' theory ($D = 1 \times 10^{3 \pm 0.3}\ nm^2/s$). Fitting the transit time distributions to Eq. 3 (Fig. 4B, solid lines) and Eq. 4 (Fig. 4B, dashed lines), ω_K was again similar for both folding and unfolding. The result, $\omega_K = 3 \pm 1 \times 10^3\ s^{-1}$, implied $D = 1.3 \pm 0.6 \times 10^3\ nm^2/s$, in excellent agreement with the result found from the rates and landscape reconstruction using Kramers' theory (*25*). However, the barrier height returned by the fit, $\Delta G^{\ddagger} = 0.5 \pm 0.3\ k_B T$, was once again lower than the measured value, because (as for the hairpin) more short transit times were observed than would be expected from the 1D harmonic theory.

For both molecules, the transit time distributions thus agreed reasonably well with the expectations from 1D harmonic approximations to the previously measured landscapes. The primary discrepancy was a slight bias in the transit time distributions toward shorter times, which caused the fitted barrier height to be lower than the measured height. This bias might arise from a breakdown in the approximations used to derive Eq. 3 (*21*), such as anharmonicity in the barriers or the need to include higher dimensionality in the landscape, or it could reflect the influence of the dynamics of the beads and handles to which the molecules are tethered (*23*, *26*–*28*), which were not included in the analysis because they are difficult

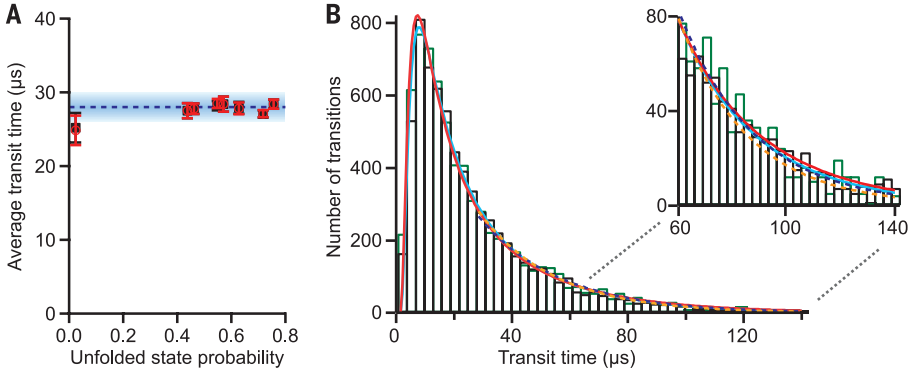

Fig. 3. Transit times for a DNA hairpin. (**A**) The measured average transition path time (blue) agrees very well with the values predicted by Eq. 2 for folding (red) and unfolding (black) over a range of forces from low (hairpin mostly folded) to high (hairpin mostly unfolded). Error bars represent SEM. (**B**) The distribution of transit times for barrier crossing is the same for both folding (green) and unfolding (black) transitions. The full distributions are well fit by Eq. 3 (red, unfolding; cyan, folding) and the tails (inset) are separately well fit by Eq. 4 (orange, unfolding; blue, folding), with both fits returning the same results within error.

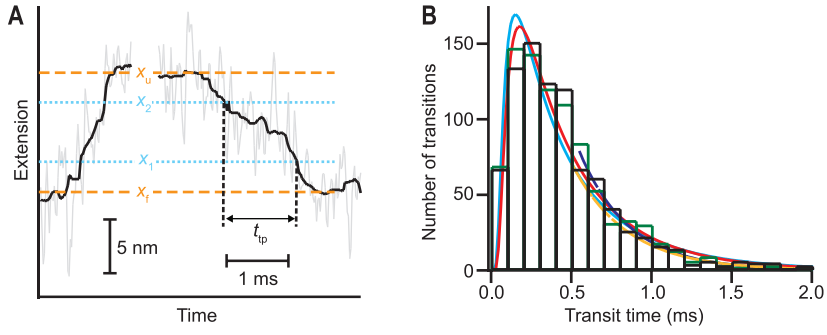

Fig. 4. Transition paths and transit times for a protein. (**A**) Slow folding of dimeric PrP produced transit times on the milisecond time scale [black, extension trajectories filtered in a 0.4-ms window; gray, unfiltered trajectories; orange, extensions of folded (x_f) and unfolded (x_u) states]. Cyan, boundaries x_1 and x_2 defining the barrier region. (**B**) The distribution of transit times for barrier crossing is the same for both folding (green) and unfolding (black) transitions. The full distributions are both well fit by Eq. 3 (red, unfolding; cyan, folding) and the exponential tails are separately well fit by Eq. 4 (orange, unfolding; blue, folding).

to treat (*28*). The fact that values of the diffusion coefficient (a fundamental descriptor of the dynamics) obtained from different experimental variables using 1D theories are similar suggests that these 1D descriptions of folding (*8*, *11*, *14*, *19*, *29*) can hold even at the microscopic level, despite their many simplifying assumptions.

The ability to observe and characterize transition paths opens up many exciting avenues to explore in folding studies by allowing more direct investigation of transition states and the microscopic thermally driven motions that underlie the conformational search. Previously invisible microstates along the transition paths may now be detectable, permitting their properties to be characterized directly. Moreover, it may be possible to distinguish different classes of transition paths having different properties, such as barrier heights, intermediates, or roughness. The potential for deeper integration of experiment and simulation through direct comparisons of the transition path properties found experimentally to the results of atomistic simulations is also exciting (*4*). Because the transit time is so sensitive to the diffusion coefficient D (*4*, *6*, *23*), such measurements also hold great promise for investigating the effects of solvent viscosity and internal friction (*4*, *6*, *30*).

REFERENCES AND NOTES

1. J. D. Bryngelson, P. G. Wolynes, *Proc. Natl. Acad. Sci. U.S.A.* **84**, 7524–7528 (1987).
2. J. Buchner, T. Kiefhaber, Eds., *Protein Folding Handbook* (Wiley-VCH, Weinheim, Germany, 2005).
3. P. G. Bolhuis, D. Chandler, C. Dellago, P. L. Geissler, *Annu. Rev. Phys. Chem.* **53**, 291–318 (2002).
4. H. S. Chung, S. Piana-Agostinetti, D. E. Shaw, W. A. Eaton, *Science* **349**, 1504–1510 (2015).
5. H. S. Chung, K. McHale, J. M. Louis, W. A. Eaton, *Science* **335**, 981–984 (2012).
6. H. S. Chung, W. A. Eaton, *Nature* **502**, 685–688 (2013).
7. H. S. Chung, J. M. Louis, W. A. Eaton, *Proc. Natl. Acad. Sci. U.S.A.* **106**, 11837–11844 (2009).
8. K. Truex, H. S. Chung, J. M. Louis, W. A. Eaton, *Phys. Rev. Lett.* **115**, 018101 (2015).
9. D. B. Ritchie, M. T. Woodside, *Curr. Opin. Struct. Biol.* **34**, 43–51 (2015).
10. K. Neupane *et al.*, *Phys. Rev. Lett.* **109**, 068102 (2012).
11. H. Yu *et al.*, *Proc. Natl. Acad. Sci. U.S.A.* **109**, 14452–14457 (2012).
12. M. T. Woodside, S. M. Block, *Annu. Rev. Biophys.* **43**, 19–39 (2014).
13. R. B. Best, G. Hummer, *Proc. Natl. Acad. Sci. U.S.A.* **102**, 6732–6737 (2005).
14. K. Neupane, A. P. Manuel, J. Lambert, M. T. Woodside, *J. Phys. Chem. Lett.* **6**, 1005–1010 (2015).
15. M. T. Woodside *et al.*, *Proc. Natl. Acad. Sci. U.S.A.* **103**, 6190–6195 (2006).
16. M. T. Woodside *et al.*, *Science* **314**, 1001–1004 (2006).
17. A. N. Gupta *et al.*, *Nat. Phys.* **7**, 631–634 (2011).
18. M. C. Engel, D. B. Ritchie, D. A. N. Foster, K. S. D. Beach, M. T. Woodside, *Phys. Rev. Lett.* **113**, 238104 (2014).
19. A. P. Manuel, J. Lambert, M. T. Woodside, *Proc. Natl. Acad. Sci. U.S.A.* **112**, 7183–7188 (2015).
20. Materials and methods are available as supplementary materials on *Science* Online.
21. S. Chaudhury, D. E. Makarov, *J. Chem. Phys.* **133**, 034118 (2010).
22. P. Hänggi, P. Talkner, M. Borkovec, *Rev. Mod. Phys.* **62**, 251–341 (1990).
23. M. T. Woodside, J. Lambert, K. S. D. Beach, *Biophys. J.* **107**, 1647–1653 (2014).
24. G. Hummer, *J. Chem. Phys.* **120**, 516–523 (2004).
25. H. Yu *et al.*, *Proc. Natl. Acad. Sci. U.S.A.* **112**, 8308–8313 (2015).
26. M. Hinczewski, Y. von Hansen, R. R. Netz, *Proc. Natl. Acad. Sci. U.S.A.* **107**, 21493–21498 (2010).
27. P. Cossio, G. Hummer, A. Szabo, *Proc. Natl. Acad. Sci. U.S.A.* **112**, 14248–14253 (2015).
28. G.-M. Nam, D. E. Makarov, *Protein Sci.* **25**, 123–134 (2016).
29. W. Zheng, R. B. Best, *J. Phys. Chem. B* **119**, 15247–15255 (2015).
30. A. Borgia *et al.*, *Nat. Commun.* **3**, 1195 (2012).

ACKNOWLEDGMENTS

We thank D. Makarov and A. Szabo for helpful discussions. This work was supported by the Alberta Prion Research Institute, Alberta Innovates (AI) Technology Futures, AI Health Solutions, the Natural Sciences and Engineering Research Council, and National Research Council Canada. M.T.W., K.N., and D.R.D. designed the research; F.W. provided new reagents; K.N., D.A.N.F., and H.Y. performed measurements; K.N., D.R.D., and M.T.W. analyzed the data; and M.T.W., K.N., D.R.D., D.A.N.F., and H.Y. wrote the paper.

SUPPLEMENTARY MATERIALS

www.sciencemag.org/content/352/6282/239/suppl/DC1
Materials and Methods
Fig. S1
References (*31*–*36*)

20 July 2015; accepted 18 February 2016
10.1126/science.aad0637

CANCER

SCS macrophages suppress melanoma by restricting tumor-derived vesicle–B cell interactions

Ferdinando Pucci,[1]* Christopher Garris,[1,2] Charles P. Lai,[3]† Andita Newton,[1] Christina Pfirschke,[1] Camilla Engblom,[1,2] David Alvarez,[4] Melissa Sprachman,[1] Charles Evavold,[1,2] Angela Magnuson,[1] Ulrich H. von Andrian,[4] Katharina Glatz,[5] Xandra O. Breakefield,[3] Thorsten R. Mempel,[6] Ralph Weissleder,[1] Mikael J. Pittet[1]‡

Tumor-derived extracellular vesicles (tEVs) are important signals in tumor–host cell communication, yet it remains unclear how endogenously produced tEVs affect the host in different areas of the body. We combined imaging and genetic analysis to track melanoma-derived vesicles at organismal, cellular, and molecular scales to show that endogenous tEVs efficiently disseminate via lymphatics and preferentially bind subcapsular sinus (SCS) CD169$^+$ macrophages in tumor-draining lymph nodes (tdLNs) in mice and humans. The CD169$^+$ macrophage layer physically blocks tEV dissemination but is undermined during tumor progression and by therapeutic agents. A disrupted SCS macrophage barrier enables tEVs to enter the lymph node cortex, interact with B cells, and foster tumor-promoting humoral immunity. Thus, CD169$^+$ macrophages may act as tumor suppressors by containing tEV spread and ensuing cancer-enhancing immunity.

Although cancer is driven by tumor cell–endogenous genetic mutations, it is also modulated by tumor cell–exogenous interactions with host components, including immune cells (*1*). Tumor-induced host immune system activation can occur both within and away from the tumor stroma and may involve different communication signals, including soluble factors (*2*) and tumor-derived extracellular vesicles (tEVs) (*3*). tEVs are key candidate conveyors of information between cancer and host immune cells because they can travel long distances in the body without their contents degrading or diluting. tEVs may transfer surface receptors or intracellular material to different host acceptor cells (*4*–*6*); these processes have all been associated with altered antitumor immunity and enhanced cancer progression (*7*). Circulating tEVs also have diagnostic and prognostic potential, as they can be used to detect early cancer stages (*8*) and to predict overall patient survival (*4*) and treatment responses (*9*). Despite increased understanding of tEVs' importance, a critical barrier to progress in the field has been our limited ability to assess the impact of vesicles that are produced in vivo (*7*). To shift current experimental research on tEV–host cell interactions, we combined imaging and genetic approaches to track endogenously produced tEVs and their targets at different resolutions and scales.

We assessed the whole-body biodistribution of tumor-derived material in mice bearing genetically modified B16F10 melanoma tumors (B16F10-mGluc), which produce tEVs carrying membrane-bound *Gaussia* luciferase (mGluc) (*10*) (fig. S1). Quantification of tEV-bound mGluc activity in various

[1]Center for Systems Biology, Massachusetts General Hospital Research Institute, Harvard Medical School, Boston, MA 02114, USA. [2]Graduate Program in Immunology, Harvard Medical School, Boston, MA 02115, USA. [3]Department of Neurology, Massachusetts General Hospital Research Institute, Harvard Medical School, Charlestown, MA 02129, USA. [4]Department of Microbiology and Immunobiology, Harvard Medical School, Boston, MA 02115, USA. [5]Institute of Pathology, University Hospital Basel, 4031 Basel, Switzerland. [6]Center for Immunology and Inflammatory Diseases, Massachusetts General Hospital Research Institute, Harvard Medical School, Charlestown, MA 02129, USA.
*Present address: Torque Therapeutics Inc., Cambridge, MA 02142, USA. †Present address: Institute of Biomedical Engineering, National Tsing Hua University, Hsinchu, Taiwan. **‡Corresponding author. E-mail: mpittet@mgh.harvard.edu**

Direct observation of transition paths during the folding of proteins and nucleic acids

Krishna Neupane *et al.*

Science **352**, 239 (2016);
DOI: 10.1126/science.aad0637